Water-Rock Interactions, Ore Deposits, and Environmental Geochemistry: A Tribute to David A. Crerar
© The Geochemical Society, Special Publication No. 7, 2002
Editors: Roland Hellmann and Scott A. Wood

Probing molecular-scale adsorption and dissolution-growth processes using nonlinear optical and scanning probe methods suitable for hydrothermal applications

STEVEN R. HIGGINS[1*], ANDREW G. STACK[1], KEVIN G. KNAUSS[2], CARRICK M. EGGLESTON[1], GUNTRAM JORDAN[3]

[1]Department of Geology and Geophysics, University of Wyoming, Laramie, Wyoming 82071-3006 USA
[2]L-202, Geosciences and Environmental Technology, Lawrence Livermore National Laboratory
Livermore, California 94550 USA
[3]Institut für Mineralogie, Ruhr-Universität Bochum, 44780 Bochum, Germany

* corresponding author: shiggins@uwyo.edu

Abstract—Experimental hydrothermal geochemistry has made great strides on the basis of stoichiometric equilibrium studies, measured kinetic rates, and bulk-sensitive spectroscopic data, but there are current problems in hydrothermal geochemistry ranging from deep aquifer chemistry to nuclear waste tank chemistry that can benefit from new techniques able to provide direct spectroscopic and microscopic information about processes operative at mineral surfaces. We present and discuss applications of two inherently interface-sensitive techniques that are amenable to application in hydrothermal experimentation: optical second harmonic generation (SHG) and hydrothermal atomic force microscopy (HAFM). Results of experimental SHG from a corundum-water interface are presented, along with a model relating SHG signal in part to the structure of water in the electric double layer. Although the SHG signal is closely related to surface potential, direct extraction of surface potential over a wide range of pH and ionic strength will depend upon better understanding of water structure near oxide-water interfaces. We present applications of HAFM to dissolution and growth of barite, and in particular show that the velocity and spacing of kink sites along [010] and [120] steps can be extracted from the HAFM imagery using a simple step model. The model enables us to conclude that although steps may appear straight in AFM images, the atomic scale roughness can be large, giving rise to kinks at a large percentage of step sites. Both techniques are promising ways to extend our ability to probe and better understand the nature of mineral-water interface chemistry.

1. INTRODUCTION

Chemical processes occurring at mineral-water interfaces are central to understanding how geologic materials regulate and modulate the chemical environment in which we all live. Many of these interactions occur at the Earth's surface where temperatures and pressures do not differ greatly from those with which we have direct experience, but many also occur in deep aquifers, sediments, hydrocarbon reservoirs, buried radioactive waste tanks, and geothermal systems that are considerably more experimentally challenging.

A primary tool of hydrothermal geochemistry appropriately continues to be the analysis of aqueous solutions from "quenched" field samples or from either static or flow-through laboratory experiments in order to gain information about chemical equilibrium or about reaction rates in particular systems.

Increasingly, geochemists must confront questions related to the kinetics and mechanisms of mineral-water interactions. Indirect wet-chemical methods remain a primary tool, but we need additional information to reliably interpret such data. For example, given a set of macroscopic concentration and stoichiometry data, there are often several models (e.g., diffuse layer or triple layer; single site or two site models) that apply more or less equally well (Westall and Hohl, 1980) but that differ in the surface structures implied. Interface-sensitive spectroscopic and microscopic techniques, judiciously applied, can allow us to test hypotheses pertaining to reaction mechanisms. Further, such direct information often shows that no existing model captures the complexity of the processes found to be in operation.

Many spectroscopic techniques have been applied to better understanding the nature of mineral-water interaction in aqueous systems (e.g., electronic and vibrational spectroscopies (Buckley and Woods, 1994; Hug and Sulzberger, 1994; Ainsworth et al., 1998; Eggleston et al., 1998), as well as X-ray diffraction and absorption techniques (Bargar et al., 1997; Cheng et al., 1997), white light interferometry (Lüttge et al., 1999), and nuclear magnetic resonance (NMR) (Casey et al., 2000)). However, there is a lack of techniques that are both 1) inherently sensitive to the solid-water interface rather than to the bulk of the material, and 2) amenable to direct in-situ application, particularly within hydrothermal

experiments. In this paper, we describe two techniques that are relatively new to geochemistry and that satisfy both of these requirements. These are the laser-based technique of optical second harmonic generation (SHG) (for a review, see Corn and Higgins, 1994), and hydrothermal atomic force microscopy (HAFM) (Higgins et al., 1998b). We describe how each technique works, and give examples of the kinds of information that have been, and can be, obtained from them.

SHG can be used to study the adsorption of both organic and inorganic species to mineral surfaces; we choose to concentrate here on the pH dependence of SHG from an alumina-water interface. Prior work by Ong et al. (1992) demonstrated that SHG is a viable and direct probe of interface potential, particularly for the silica/water interface. In this work, we apply this same idea to a corundum/water interface to determine if the potential-sensitive SHG mechanism is appropriate for other interfaces. The results show that relatively direct measures of surface potential may be made without the need to "filter" stoichiometric and charge-density data through models that relate charge to potential. These results however, are not free of uncertainties in that the location of a true point of zero charge requires a rather simple SHG mechanism, whereas our results suggest the mechanism may be more complicated.

In the HAFM section, we show how direct in-situ imaging of step motion on barite ($BaSO_4$) surfaces allows us to extract information pertaining to the rates and mechanisms of such microscopic processes as the motion of kink sites along steps during dissolution or growth. In general, the results point the way to improving upon long-standing equilibrium- and diffusion-based models of crystal growth (e.g., Burton et al., 1951; Chernov, 1963b).

The two experimental methods above can be used to obtain complementary information that could ultimately lead to more consistent descriptions of specific mineral-water interfaces. Resonant SHG can provide adsorbate coverage information regardless of the dynamics of the system, and thus, presents itself as a useful tool for testing the equilibrium assumption associated with modeling a net reaction rate using equilibrium surface complexation models. Whereas SHG provides important information on the adsorption of aqueous constituents, HAFM, as we will discuss below, provides dynamic information down to the molecular level (within the confines of a particular step kinetic model). As both methods are suitable for investigations under identical experimental conditions, it should be possible to make direct correlation between adsorption data from SHG and dynamic data from HAFM.

2. SECOND HARMONIC GENERATION (SHG)

2.1. SHG Theory

The electric field portion of light at a fixed location varies sinusoidally with time, creating an AC polarization of the electron cloud of a molecule exposed to it. If the magnitude of the electric field is small, the electron cloud behaves harmonically. That is, as the magnitude of the electric field changes, there is a proportional change in the position of the electrons. If the incident light's electric field is large, such as that created by a high power laser, the resulting polarization can be anharmonic and include a significant component with twice the incident light's frequency. This component is known as the second-order polarization, $P^{(2)}(2\omega)$. As an oscillating electric charge, $P^{(2)}(2\omega)$ leads to generation of light with twice the incident light's frequency. $P^{(2)}(2\omega)$ can be described as:

$$E(2\omega) \propto P^{(2)}(2\omega) = \chi^{(2)}\ E(\omega)E(\omega) \qquad (1)$$

where $E(2\omega)$ is the second harmonic field strength at frequency 2ω, $E(\omega)$ is the incident light field (at frequency ω), and $\chi^{(2)}$ is the non-linear susceptibility:

$$\chi^{(2)} = n_s\left\langle \alpha^{(2)} \right\rangle \qquad (2)$$

where n_s is the surface concentration of molecules and $\alpha^{(2)}$ is the second-order polarizability (or hyperpolarizability) of the molecules; $\alpha^{(2)}$ is a third-rank tensor and is averaged over the molecular orientation distribution denoted by the brackets.

Within the electric dipole approximation, SHG is forbidden in a centrosymmetric phase because induced polarizations will be equal in opposite directions and destructively interfere. Thus, all elements of Eqn. 2 above would be zero if the molecules were randomly oriented in the bulk phase in which the driving fields (fundamental light at frequency ω) exist. At an interface between two centrosymmetric phases, however, the centrosymmetry is broken and SHG is allowed. This imparts to SHG its inherent interface sensitivity in otherwise centrosymmetric systems.

The polarizabilities, and thus the $\chi^{(2)}$ of a given collection of molecules, is a function of the energy of the light interacting with them. Near energies at which a given molecule has an optical resonance due to transitions between electronic states, the electron cloud (or part of it) may be thought of as more deformable than at energies far from resonance. The electronic polarizabilities that give rise to SHG thus also tend to be relatively large near optical absorption energies. It is then possible to enhance the SHG signal by tuning the input laser light such that the SH

light generated occurs at a wavelength where the subject molecule has an absorption band. This sets up resonance between the electronic transition at a particular energy and the polarization of electrons at the *second harmonic* (rather than primary) frequency (Corn and Higgins, 1994).

Often, however, resonant SHG is not possible. In the case of the oxide-water interfaces discussed below, there is negligible optical absorption at frequencies used in the experiments. This type of experimental arrangement is usually referred to as non-resonant SHG and commonly a total internal reflection (TIR) experimental geometry is employed. In this case, the evanescent electric field associated with light undergoing TIR from an interface can give rise to enhanced SHG (Ong et al., 1992; Conboy et al., 1994). The TIR geometry restricts the range of solid-water interfaces that can be probed because the input laser light must approach the interface from the side that is optically more dense. This is most often from the solid side, requiring an optically transparent single crystal (or amorphous material) of up to centimeter dimensions. The source of SHG from these non-resonant systems is often ascribed to the static electric field at the interface (Ong et al., 1992; Lantz et al., 1993; Lantz and Corn, 1994). However, it is important to clarify that it is not the static field that gives rise to the SHG, but that there is some material property that changes with the static field. Thus, it may be more correct to state that the non-linear susceptibility of the material, immersed in the field, changes with the field strength. For the case of aqueous interfaces, it is believed that the orientation of the water molecules in the static field gives rise to a significant contribution to the non-linear susceptibility of the interface (Ong et al., 1992; Zhao et al., 1993a).

Resonant SHG can be used to probe the relative amounts of, as well as the average orientation of, organic molecules adsorbed at interfaces given appropriate molecular characteristics (i.e., large non-linear molecular polarizability). In recent work, we have used SHG to study the adsorption of rhodamine dye molecules to single-crystal corundum surfaces (Higgins et al., 1998d; Higgins and Eggleston, submitted). Other studies of dye molecule adsorption to various fused silica interfaces have appeared in the literature (e.g., Heinz et al., 1982; 1983; Higgins et al., 1991; Kikteva et al., 1999). These studies demonstrate how Eqns. 1 and 2 may be utilized for determining the average molecular orientation of the adsorbates. A recent paper by Simpson and Rowlen (1999), however, point out some potential flaws in the assumptions associated with molecular orientation calculations. Aside from dye molecules, whose large non-linear polarizabilities make them attractive for SHG studies, many adsorption studies of para-substituted benzene have been successful due to large changes in the molecular dipole moment associated with electronic transitions (e.g., Bhattacharyya et al., 1987; Castro et al., 1991; Higgins et al., 1992; Zhao et al., 1993b).

Recent SHG developments have shown that SHG may also probe the surfaces of particle suspensions, opening up the potential applications of SHG to a large variety of mineral-water interfaces (Wang et al., 1996; Yan and Eisenthal, 2000). Here, however, we concentrate instead on the pH-dependence of SHG from amorphous silica-water and corundum-water interfaces. As mentioned above, this type of study is best performed in the TIR geometry owing to the non-resonant relationship between the interface and the fundamental and second harmonic fields. The TIR geometry may only be applied through bulk solids of optical quality and minimal absorption at the frequencies employed.

2.2. pH Dependence of SHG from the Oxide-Water Interface

Figure 1 shows the experimental TIR configuration we used to obtain SHG from oxide-water interfaces. Laser light impinges on the oxide-water interface from the solid side, through a prism comprising the mineral of interest (e.g., silica or corundum). Further experimental detail is presented elsewhere (Stack et al., 2001).

Figure 2 shows the SHG amplitude from a fused silica-water interface as a function of pH. The SHG intensity rises as pH rises, but unevenly; relatively abrupt rises in signal occur at pH < 2, pH ≅ 4.5, and pH ≅ 8. Our measurements were intended to, and indeed do, reproduce the pH-dependent results of Ong et al. (1992) for an amorphous silica/water interface. These authors proposed a model in which the second-order polarization of the interface, $P^{(2)}(2\omega)$, is the sum of a pH-independent baseline and a pH- and ionic strength-dependent component:

$$E(2\omega) \propto P^{(2)}(2\omega) = \chi^{(2)} E(\omega)E(\omega) + \chi^{(3)} E(\omega)E(\omega)\Psi_0 \qquad (3)$$

where $E(2\omega)$ is the second harmonic field, $E(\omega)$ is the field of the fundamental light and contains the Fresnel coefficients relevant to the particular experimental geometry employed (Mizrahi and Sipe, 1988), Ψ_0 is the potential at the interface relative to the bulk solution, and $\chi^{(2)}$ and $\chi^{(3)}$ are second- and third-order non-linear susceptibilities, respectively. The $\chi^{(2)}$ term is considered by Ong et al. (1992) and Zhao et al. (1993a) to be independent of pH and ionic strength. The $\chi^{(3)}$ term accounts for a static electric field con-

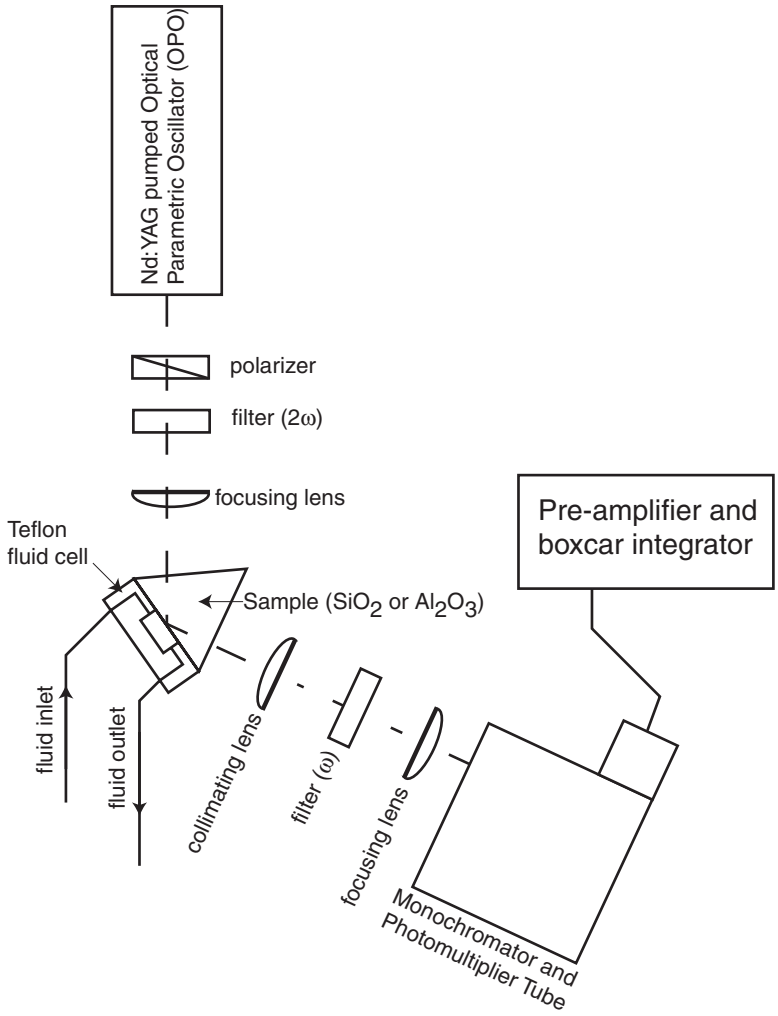


Fig. 1. Experimental configuration for total internal reflection (TIR) SHG investigation of oxide water interfaces.

tributing to the SHG due to Ψ_0. $\chi^{(3)}$ is attributed to water molecules in the diffuse layer that are oriented by the static interfacial electric field.

Equation 3, with the assumptions that $\chi^{(2)}$ and $\chi^{(3)}$ are constant, provides a way of directly probing oxide surface potentials without the need to interpret stoichiometric (surface charge density) data via various possible physical models of the electric double layer. Extracting a surface potential, however, requires a method for determining $\chi^{(3)}$ through variation of Ψ_0. Thus, in order to determine $\chi^{(3)}$ initially, a specific potential-charge density relationship must be applied as a calibration. It has been shown that a determination of $\chi^{(3)}$ by this approach yields model-independent potential measurements for the silica-water interface (Ong et al., 1992). Equation 3 can be solved for Ψ_0 if $\chi^{(2)}$ and $\chi^{(3)}$ are known and are pH-independent, but the assumptions may be questionable. The $\chi^{(3)}$ term, for example, depends upon the overall structure of water in the interfacial region. If the average water orientation does not vary linearly with surface potential, then extraction of Ψ_0 from pH-dependent SHG data will depend upon models of interfacial water structure—an area of current and sometimes controversial research (Toney et al., 1994; Danielwicz-Ferchmin and Ferchmin, 1996).

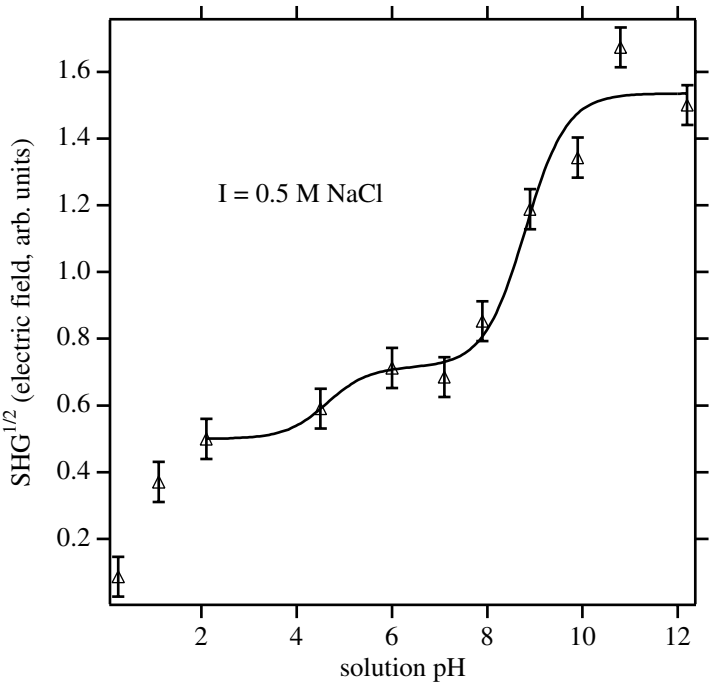


Fig. 2. SH field strength, $E(2\omega)$, vs. pH for the amorphous silica/water interface. The fit was calculated using an acid-base species distribution function.

Whether linear or not, however, it is clear that the surface electric field created by the development of surface charge at high pH also leads to increased SHG at high pH (Fig. 2). Given that $\Psi_0 = 0$ at the pH of point of zero charge (PZC) of silica, then all of the SHG signal at the PZC can be attributed to the $\chi^{(2)}$ term of Eqn. 3. The PZC of amorphous silica is in the pH range 2-3.5 (Parks, 1965; 1990; Sahai and Sverjensky, 1997). Assuming that $\chi^{(2)}$ is indeed pH independent (Ong et al., 1992), then increases in SHG with increased pH are directly proportional to the surface potential Ψ_0 developed as the silica develops negative charge by deprotonation of silanol groups. The relatively abrupt rises in SHG field strength occur at pH values corresponding to the pK_a of surface silanol groups. Ong et al. (1992) determined pK_a values of 4.5 and 8.5, and from our data we obtain comparable values of 4.6 and 8.8 on the basis of fitting of the SHG data to a typical monoprotic acid-base equilibrium. However, it must be emphasized that these surface pK_a values are obtained on the basis of assumptions that remain to be validated.

The lowest pH value explored by Ong et al. (1992) was 2. This is roughly coincident with the amorphous silica PZC. Our data (Fig. 2) show that the SHG signal continues to decrease at pH values below 2, suggesting a protonation reaction with a pK_1 less than 2. This is consistent with reported values for amorphous silica of $pK_1 < 0$ (e.g., Sverjensky and Sahai, 1996). Despite the fact that $|\Psi_0|$ increases as pH increases or decreases away from the PZC, there is no minimum in the SHG signal at the PZC. This can be understood by consideration of the phase relations between different sources of SHG. As the sign of the electric field at the interface changes about the PZC, the phase of SH light due to this static electric field undergoes a 180 degree phase shift. If the static field generated the only source of SH light, then the PZC should correspond to the minimum in SH field strength. However, in Fig. 2, the SH field is not zero at the PZC for silica, so generally, we must regard the phase relationship between multiple sources of SH light.

We turn to our results for SHG from a corundum-water interface to examine these phase relations. Using the same experimental configuration shown in Fig. 1, but replacing the fused silica prism with a corundum prism, we measured the SHG field strength as a function of bulk pH and ionic strength. We assume that the corundum-water interface is hydroxylated (Laiti et al., 1998).

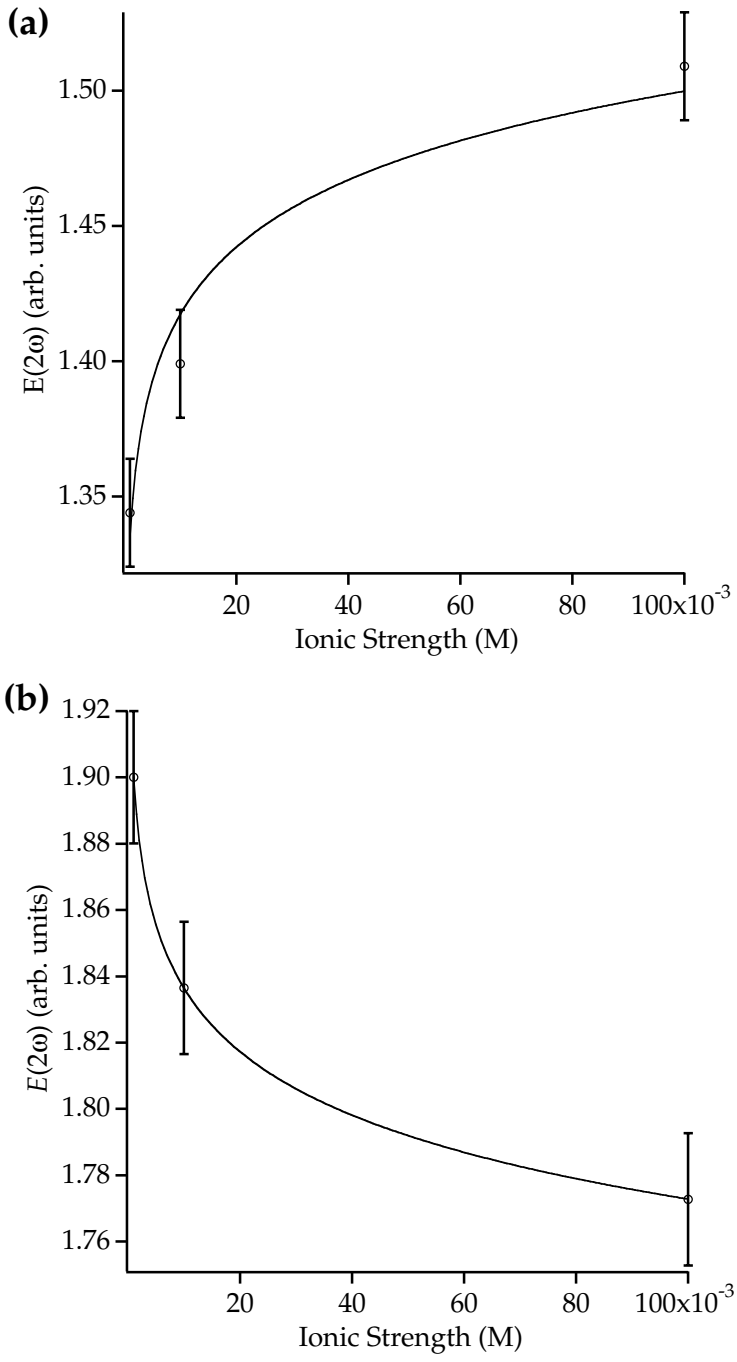


Fig. 3. SH field strength, $E(2\omega)$, as a function of ionic strength for the corundum-water interface. (a) NaCl supporting electrolyte, pH = 3.5. (b) $NaNO_3$ supporting electrolyte, pH = 10.5. The solid lines are two parameter fits to Eqn. 4 using the diffuse layer model for the surface potential (Zhao et al., 1993b).

Figure 3 shows the ionic strength dependence of $E(2\omega)$ from the corundum-water interface at pH 10.3 for $NaNO_3$ electrolyte and pH 3.5 for NaCl electrolyte. We fit the data in Fig. 3 to Eqn. 4, which is functionally equivalent to Eqn. 3 (Zhao et al., 1993b), using the Gouy-Chapman diffuse-layer model for Ψ_0.

$$E(2\omega) = A + B\Psi_0 \quad (4)$$

By choosing extreme pH values, relative to the observed point of zero salt effect (PZSE), for fitting $E(2\omega)$ vs. ionic strength, we assume that the corundum surface charge is near or at the maximum surface charge density, $\sigma \cong \sigma_{max}$. Figure 4 shows some of our results for both the pH and ionic strength dependence of SHG from the corundum-water interface. Using the parameters A, B, and σ_{max} from fitting the Fig. 3 data, Ψ_0 was found as a function of pH as shown on the right-hand axis of Fig. 4. For the NaCl electrolyte, A = 1.9, B = -0.072 ± 0.014, and $\sigma_{max} = 1.4 \pm 1.8$ C m^{-2}, whereas for the $NaNO_3$ electrolyte, A = 1.5, B = 0.055 ± 0.006, and $\sigma_{max} = 0.7 \pm 0.8$ C m^{-2}. On both plots in Fig. 4, we have superimposed a line with slope equal to 59.2 mV per pH unit. This slope is expected for the data if the surface protonation reaction can be regarded as potential-determining. The data in both plots have similar slope to the superimposed lines, indicating consistency between the observations and the expected Nernstian behavior of the oxide/water interface.

Aside from the Nernstian behavior, the general trends in the data offer additional points for discussion. As for silica, $E(2\omega)$ increases with pH. In $NaNO_3$ solution, at high pH, $E(2\omega)$ decreases with increasing ionic strength, while at low pH, $E(2\omega)$ increases with increasing ionic strength, though not as markedly. In NaCl solution, at low pH, $E(2\omega)$ increases with increasing ionic strength, but shows no apparent ionic strength dependence for pH > 6. A crossing point of the $NaNO_3$ data allowed us to estimate a PZSE in the region 4 < pH < 6. However, there is no clear crossing point for the NaCl data.

Zhao et al. (1993a) measured the ionic strength dependence of SHG from two similar air-water interfaces to which positively or negatively charged organic molecules had been adsorbed, and found that the direction of the ionic strength dependence reverses with the sign of the charge of the interface. This behavior is attributed to constructive or destructive interference between the $\chi^{(2)}$ and $\chi^{(3)}$ terms of Eqn. 3, an idea supported by Du et al. (1994) who showed that the phase of the sum-frequency generation (SFG) signal from a silica-water interface shifts by 180° between high and low pH. This is as expected from the "flip" of near-surface water molecules from oxygen-down at low pH (positive surface charge) to oxygen-up at high pH (negative surface charge). Such light can interfere constructively or destructively with the fixed-phase light of the $\chi^{(2)}$ term in Eqn. 3.

Thus, the data suggest that at high pH (pH > PZSE), constructive interference between the $\chi^{(2)}$ and $\chi^{(3)}$ terms of Eqn. 3 leads to a relatively large SHG signal. As the ionic strength increases and the depth of the electric double layer decreases, fewer water molecules contribute to SHG via the $\chi^{(3)}$ term and the signal decreases. At pH < PZSE, destructive interference between the $\chi^{(2)}$ and $\chi^{(3)}$ terms leads to relatively small SHG signal. As the ionic strength increases and the depth of the electric double layer decreases, fewer water molecules contribute to SHG via the $\chi^{(3)}$ term and the signal increases because there is *less* destructive interference.

2.3. SHG Model Discussion

One of the main problems with the data in Fig. 4 is the discrepancy between PZSE values for the two electrolytes. Whereas in the NaCl electrolyte a PZSE cannot be discerned above pH ≅ 6, in the $NaNO_3$ electrolyte the PZSE appears at pH ≅ 5. In the absence of specific electrolyte complications to the surface chemistry, or to the surface non-linear susceptibility, the PZSE should correspond to the PZC and is generally accepted to be at pH ≅ 9.3 for α-alumina (Davis and Kent, 1990; Sverjensky, 1994). The NaCl data therefore, are not inconsistent with this literature value. However, Stack et al. (2001) found that AFM force-distance measurements are inconsistent with a PZC of this corundum prism surface located at pH ≅ 9.3. If we accept that the literature value of the PZC for corundum is applicable to this particular interface, the $NaNO_3$ data require further discussion to attempt to examine the model deficiencies. The assumption that the electrolyte concentration only affects the ionic strength may not be valid for $NaNO_3$ if the non-linear polarizability of NO_3^- is non-negligible. If this were true, we would expect the SHG model to deviate at low pH where the positive surface charge will cause a higher concentration of NO_3^- ions at the interface. The result of this additional SHG mechanism will be to shift the observed PZSE from the true PZC. The direction of the shift will depend upon the phase of the SH light generated by the ions. Regardless of the phase, if the NO_3^- ions are contributing to the surface non-linear susceptibility, then the assumption that the $\chi^{(2)}$ term is independent of pH and ionic strength is invalid because the NO_3^- polarizability will contribute to this term. The observed PZSE at pH ≅ 5 suggests that if the NO_3^- contribution dominates

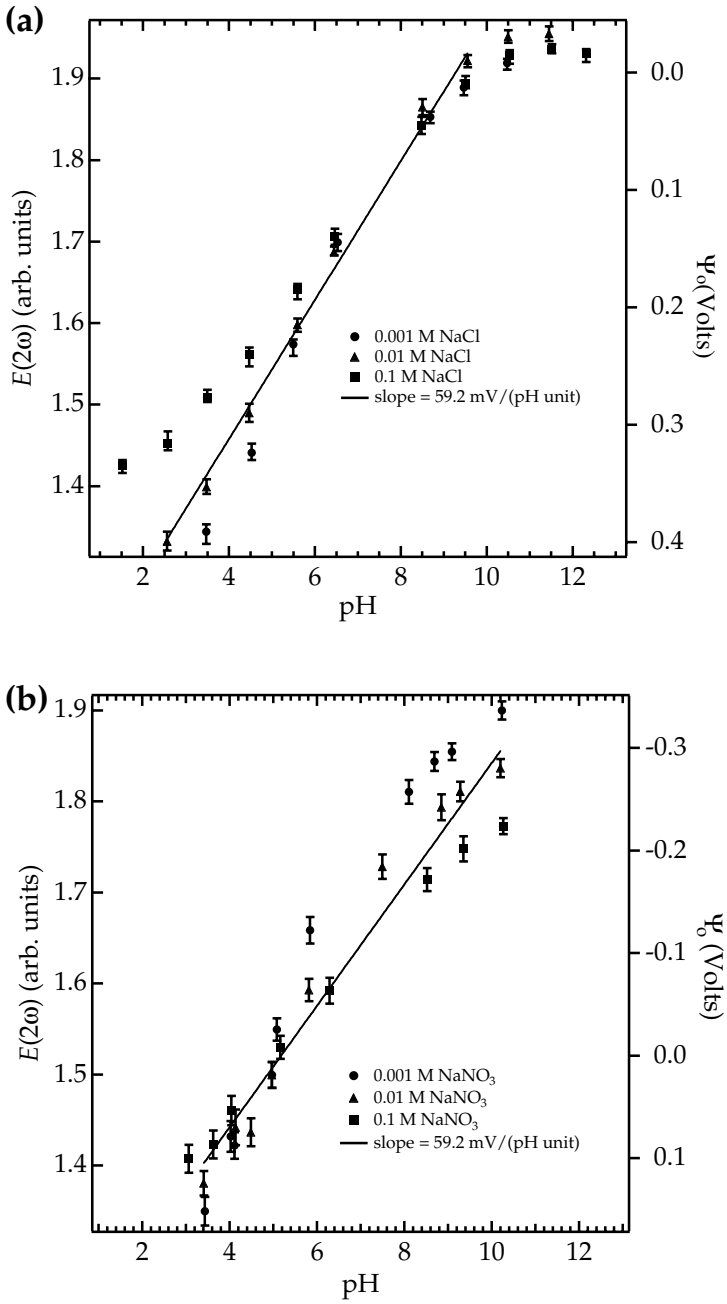


Fig. 4. SH field strength, $E(2\omega)$, as a function of pH for 3 different ionic strengths of (a) NaCl and (b) $NaNO_3$. The right hand axes in both figures correspond to the surface potential determined by the fitting parameters from Fig. 3.

$\chi^{(2)}$ at low pH, it would be 180° out of phase with respect to the $\chi^{(3)}$ term.

The $\chi^{(3)}$ term will be a function of the number of water molecules oriented, their average orientation, and a static electronic polarization stemming from the surface potential. Following Gragson et al. (1997), we propose that $\chi^{(3)}$ of Eqn. 3 cannot be assumed a constant at high surface potentials. This amounts to as-

serting that near-surface water molecules, once aligned (dipole oriented) by a surface electric field, cannot become *more* aligned with higher potentials. To address these possible model shortcomings, information regarding the interfacial water structure must be provided by more direct methods such as SFG (Du et al., 1994), or far-IR absorption studies (Russell et al., 1993a,b). Until a more quantitative description of water structure at interfaces is developed, we must accept the limitations of the constant $\chi^{(3)}$ assumption.

In summary, according to available models, the PZSE of the SHG data should occur at the PZC if the model for the SHG mechanism by Ong et al. (1992) is correct. The data using NaCl as a background electrolyte was consistent with the SHG mechanism, giving an approximate change in surface potential with pH of 59 mV/pH unit. While this $\Delta\Psi/\Delta$pH value was similar for the $NaNO_3$ background electrolyte, the PZSE was found to be much lower than expected from literature data on the PZC for corundum. Thus, the $NaNO_3$ results suggest that the SHG mechanism may be more complicated than that described by the model. Clearly a better understanding of SHG mechanisms are vital to further applications of this optical method to mineral/water interfaces. With this knowledge, SHG could be used to obtain complementary information from surfaces undergoing net dissolution or precipitation reactions. Thus, it may be possible to relate surface coverage of ligands to an observed ligand-promoted dissolution rate, all under the same conditions, whereas in current experimental methods, the surface coverage information must be obtained under equilibrated conditions.

3. HYDROTHERMAL ATOMIC FORCE MICROSCOPY (HAFM)

3.1. Introduction to HAFM

Many studies of mineral dissolution and growth have been made using the capabilities provided by atomic force microscopy (AFM), also known as scanning force microscopy (SFM). Calcite has been a particularly popular target of AFM-based dissolution and growth studies primarily because of its geologic importance but also, in part, because of its relative kinetic lability. In other words, calcite dissolves and grows quickly enough to be amenable to ambient temperature AFM imaging of step motion. Such studies have provided information of unprecedented detail about calcite surface and step structure, step kinetic rate constants, activation energies for step and kink dynamics, and even thermodynamic quantities such as step energies (e.g., Gratz et al., 1993; Liang et al., 1996; Britt and Hlady, 1997; Jordan and Rammensee, 1998; Teng et al., 1998; 1999; Shiraki et al., 2000).

In practice, there is a fairly narrow range of dissolution or growth rates that can be studied using AFM. On the one hand, surface features must move far enough to be clearly distinguished from microscope drift over time or from tip-induced effects on the surface (Park et al., 1996). On the other hand, if growth or dissolution rates are sufficiently large, it is difficult to interpret surface kinetic observations without considering the probable limits of mass transport. It has been noted that for practical AFM imaging, the range of amenable dissolution or growth rates lies between 10^{-6} and 10^{-10} mol m^{-2} s^{-1} (Dove and Platt, 1996). Depending upon particular microscopes and upon the particular goals of an experiment, however, this range may be generous as the upper limit may result in mass transport limitations in unpredictable fluid flow conditions and tip influences will likely disturb measurements at the lower limit.

One consequence of this limited range of AFM accessibility is that, despite the near-molecular scale resolution capabilities of AFM, slowly-dissolving or growing minerals, including most oxides and aluminosilicates, cannot be investigated in a practical manner using commercially available AFMs that are limited to near room temperature. The key problem in approaching hydrothermal conditions with AFM is the need to pressurize a fluid cell to elevate temperatures up to and beyond the ambient-pressure boiling point of the solution. Here, we describe the design of an HAFM (Higgins et al., 1998b) capable of imaging at up to about 12 bars and 150 °C, and present results demonstrating its utility for mineral dissolution and growth experiments at elevated temperatures for barite.

Our specific hypothesis for barite is based on our previous observations of differences in the barite (001) monolayer and bilayer step velocities (Higgins et al., 1998c). In these observations, we found that when bilayer steps are formed, there remains on either end of the bilayer step, a monolayer step segment. If the formation of the bilayer step results in a new step velocity (i.e., $v_{st}(monolayer) \neq v_{st}(bilayer)$), then the monolayer segments on either end of the bilayer step should adopt a new step direction. In particular, we present results pertinent to a Kink Donation model that allows us to extract net rates of kink attachment/detachment from HAFM data for dissolving and growing barite ($BaSO_4$). With the typical room temperature growth and dissolution rates of barite falling toward the lower end of observable dissolution by AFM, we have chosen to accelerate these rates, to avoid large tip influences, through the use of elevated temperatures in the HAFM.

3.2. HAFM Design

A principal component of virtually any SFM is the piezoelectric ceramic scanner required for molecular scale, three-dimensional positioning and rastering of the sample beneath the AFM tip. Some AFMs use tracking lenses in association with a scanned tip design and keep the sample stationary, but the HAFM uses the scanned-sample design. We use a 7-electrode lateral-vertical decoupled PZT-5A tube scanner. This type of scanner significantly reduces coupling between horizontal and vertical scanner motions, and has nearly constant sensitivity between 60 and 150 °C. Piezoelectric tube scanners cannot function effectively under pressure differentials of the > 6 bars magnitude needed for imaging in aqueous solution at 150 °C, and they and their associated wiring must be physically separated from the corrosive, hot aqueous solutions of an HAFM fluid cell. These constraints require, first, that both the scanner and the fluid cell be pressurized (i.e., that the piezoelectric scanner and coarse-approach stepper motor be placed within a gas-pressurizable chamber). Second, the material used to separate the fluid cell (containing the sample) from the chamber housing the piezoelectric scanner must be flexible, have low water and gas permeability, and be inert toward hot, corrosive aqueous solutions. We have chosen a material known by its trade name as Kalrez^{TM} (a perfluoro elastomer) to form a flexible, chemically-inert membrane separating the fluid cell from the base chamber. The remainder of this section is a brief description of the HAFM fluid cell, the fluid delivery system, and discussion of recently implemented and planned improvements to the original HAFM design (Higgins et al., 1998b).

The fluid cell, detailed in Fig. 5, consists of a main cell body, a cell cover, and a sample mounting disk, all fabricated from grade 2 titanium. Fluid inlet and outlet ports are provided for flow-through experiments and a third port is available for a temperature sensor. Optical access for laser light (optical detection schemes for cantilever deflection measurements are used in most commercial systems) is provided by sealing a sapphire window to the cell cover. The cell cover also serves as the mount for the cantilever/substrate assembly. The bottom of the cell consists of the sample mounting disk and the Kalrez^{TM} membrane which additionally effects a seal of the fluid cell. We have found this fluid cell design useful for experiments ranging from a few hours to several days duration. Other than periodic calibration checks and routine cleaning, there is no additional maintenance over and above what one would expect from a commercial system.

The fluid delivery system for the HAFM permits controlled, ratioed mass flow from two reservoirs whose contents may be changed without disrupting an experiment in progress. A key to making the HAFM function consistently and nearly free of thermal drift is the control of fluid flow with a controlled leak downstream of the HAFM fluid cell using a liquid mass flow controller. Other means of controlling fluid flow with pumps are not only more expensive, but require two pressure sources that must be carefully controlled in order to keep the pressure differential across the Kalrez^{TM} membrane < 0.05 bars at all times. The HAFM design may be compared to other recent developments that allow sample and fluid cell heating (Butt et al., 1999; Workman and Manne, 2000).

3.3. HAFM Applications

We have made use of the HAFM in dissolution and/or growth studies of such mineral phases as barite (Higgins et al., 1998c; 2000a), magnesite (Jordan et al., in press), anorthite/labradorite (Jordan et al., 1999), and hematite (Higgins et al., 1998a). Some very enlightening barite dissolution and growth studies (e.g., Bosbach et al., 1998; Pina et al., 1998; Bosbach, 2002; Wang et al., 2000) using ambient temperature AFM have been reported. For example, Bosbach et al. (1998) reported that chelating agents such as ethylenediaminetetraacetate (EDTA) increased the rate of pit formation in the dissolution of barite while growth inhibitors such as nitrilotrimethylenephosphonic acid (NTMP) retarded the formation rate of monolayer islands and the growth velocity of steps. Pina et al. (1998) noted a dramatic difference in the growth velocity of straight monolayer steps along <120> on barite (001) in contrast to the approximately ten-fold higher velocity of curved steps opposite these slower, straight steps. These results indicate a marked difference in the molecular kinetics at crystallographically different steps.

In the present work, we focus on some of the subtleties associated with barite dissolution and growth that, at present, are most amenable to study using the HAFM. In particular, we are interested in gaining kinetic information on the rates of attachment and detachment at step edges, thus providing a means to discuss crystal growth and dissolution mechanisms at the molecular scale.

The experimental methods for study of barite dissolution and growth have been reported elsewhere (Higgins et al., 1998c; 2000a). Figure 6 shows a sequence of four HAFM images of dissolving barite (001) taken at 90°C with a constant flow rate of 20 g/hr of de-ionized H_2O. Using the crystallographic axes shown in Fig. 6a, it is clear that there are two principal step di-

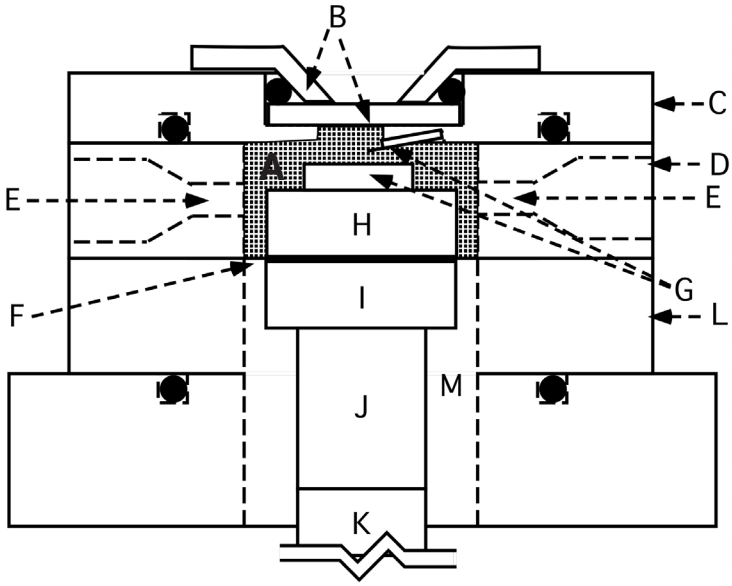


Fig. 5. Schematic of the HAFM fluid cell. Key: A. fluid environment (stippled pattern) B. sapphire window and cover C. Ti cell cover D. Ti cell body E. fluid in/out ports F. Kalrez™ membrane G. sample and cantilever/tip H. Ti sample mount I. sample mount back disk J. Macor™ spacer K. Piezoelectric ceramic scanner tube L. Kel-F™ spacer M. inert gas environment.

rections observed during dissolution under these conditions: the <010> and <120> step directions. Due to the 2_1 screw axis in barite, monolayer (3.5 Å deep) triangular-shaped pits, bounded by <120> steps on two sides and a [010] step on the third side, are oriented in opposite directions in adjacent monolayers along [001]. The <120> monolayer steps retreat at a velocity approximately 2 times greater than that of the [010] monolayer steps and as a result, the pit vertices eventually reach the monolayer [010] step of the next highest layer exposed at the surface. For example, in Fig. 6c, the pit vertex defined by intersecting <120> steps reaches the neighboring layer's [010] step, resulting in the formation of a [010] bilayer (7.1 Å height) step marked as [010]-2 in the figure. A similar process occurs in the formation of <120> bilayer steps (Higgins et al., 1998c). Both types of bilayer steps retreat at a higher velocity than the corresponding monolayer steps, with the <120> bilayer steps retreating 2.5 times faster than the [010] bilayer steps. We turn our discussion toward the fate of the remaining monolayer step segments (denoted [010]-1, in Fig. 6c for example) on either side of the bilayer steps.

Step velocity measurements on images similar to those in Fig. 6 revealed that the [010]-1 and [120]-1 step segments assume the velocity of the respective bilayer segments (Higgins et al., 1998c). From image sequences similar to that in Fig. 6, it can be shown that the monolayer step segments assume the velocity of the bilayer segment by a slight change in the monolayer step orientation.

We describe the above increase in the monolayer step velocity, or change in the monolayer step orientation by means of a Kink Donation (KD) model. In the KD model, kinks reaching the end of the bilayer segment cross the point at which the bilayer step bifurcates (labeled "A" in Fig. 7b) as donated kinks to the monolayer step segment. Thus, the rate at which kinks reach point *A* must equal the frequency of row removal (i.e., retreat rate) from the faster of the two kink sources (i.e., steps). The retreat rate of the monolayer step then is no longer governed by local processes on that segment, but by the processes governing the rate of bilayer step retreat. The increase in the monolayer step velocity then results from the misorientation of the step as shown by the dashed lines in Fig. 7. The KD model is simply a restatement of the Wulff construction in terms of anisotropy in step kinetics (Chernov, 1963a), as opposed to anisotropy in step free energy (Zangwill, 1988). The KD model is particularly useful in making quantitative estimates of the kink dynamics on barite (001). Below is a quantitative description of the KD model.

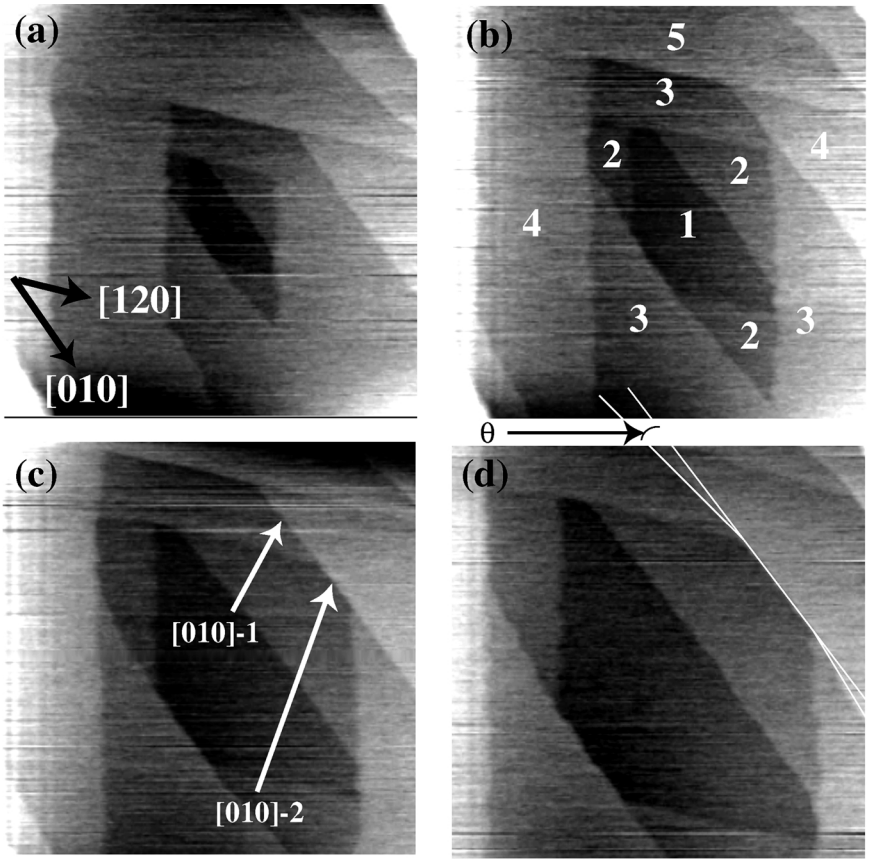


Fig. 6. Sequence of four 1.4 µm x 1.4 µm HAFM images of barite (001) taken at 90 ºC with a constant flow of de-ionized water at 20 g/hr. The time between frames was 100 sec. The predominant step orientations were [010] and [120]. The crystallographic orientation is shown in (a). In (b), the terraces are labeled in order of increasing height on the surface. Also in (b), on the right hand side of the image, a pit vertex is about to reach the adjacent layer's [010] step, resulting in the formation of a [010] bilayer step separating terraces 2 and 4 in (c). The acceleration of the newly formed bilayer step segment causes a misorientation of the monolayer step segments to either side of the bilayer segment in (d).

The kinematics of step retreat, pertinent to the KD model, are described by a simple one-dimensional nucleation and growth model. In this model, described by Lauritzen (1973) and Frank (1974), a nucleation event along a step gives rise to two dissolution/growth sites (e.g., kinks) on either side of the nucleus. The primary supposition in this mathematical treatment is that the nucleus has infinitesimally small width compared to the distance to the next kink. The subsequent growth at the kinks then takes place until either (1) the kink reaches the end of the step or (2) the kink annihilates with another kink traveling in the opposite direction. The velocity of steps, v_s, can be expressed exactly if the length density (e.g., μm^{-1}) of kinks, ρ_k, and their velocity, R_k, are known:

$$v_S = b\rho_k R_k \tag{5}$$

where b is the length, normal to the step, of one dissolution/growth unit. However, ρ_k depends upon R_k, prompting an approximate solution involving independent variables. The solution to this problem is approximated by two limiting growth regions (Frank, 1974):

$$v_s \approx \begin{cases} R_{kk} bl, & \text{region I, where } l\left(\dfrac{R_{kk}}{2R_k}\right)^{1/2} < 0.1 \\ b(2R_{kk}R_k)^{1/2}, & \text{region II, where } l\left(\dfrac{R_{kk}}{2R_k}\right)^{1/2} > 10 \end{cases} \tag{6}$$

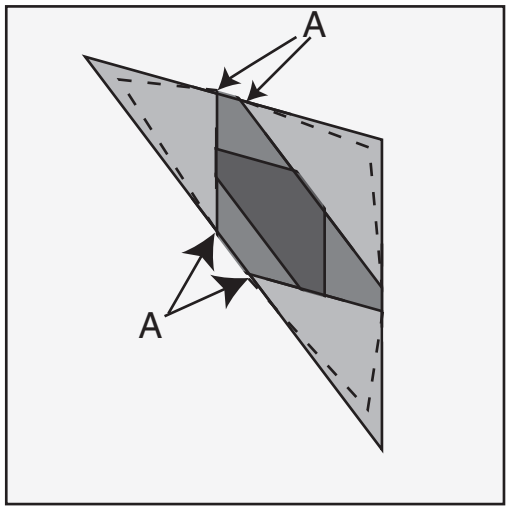


Fig. 7. Observed etch pit shape under the conditions of this study. Monolayer pit vertices are truncated due to bilayer step formation. The actual position of the monolayer step segments is depicted by the dashed lines.

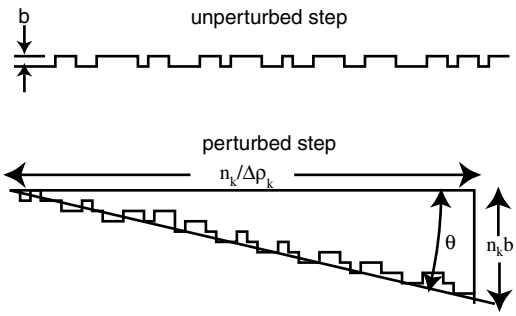


Fig. 8. Illustration of the concept of kink density perturbation.

where l is the length of the step, and R_{kk} is the nucleation rate per unit step length. The equation describing the growth region lying in between these limiting cases is not easily derived. In the step length-dependent growth region, the rate is determined by the nucleation rate. When a step becomes sufficiently long, or if $R_{kk} \approx R_k$, step velocity is nearly independent of step length, and the velocity is approximated by the geometric mean of the kink nucleation and growth rates. In this case, the growth rate is neither limited by nor determined by the nucleation rate. However, the balanced kinetics involving nucleation, growth, and annihilation, is maintained in part by nucleation events.

To understand the perturbation in the monolayer step orientation (Fig. 8), we cast our observations in terms of the KD model. We start by considering two separate growing steps, the only difference being that one step orientation is along a close-packed direction (e.g., the <120> or <010> monolayer steps) whereas the latter step orientation is vicinal relative to the former. That is, the latter step contains a certain number of donated, or excess, unidirectional kinks. Figure 8 illustrates these ideas. Assuming now that the particular kink dynamics associated with the unperturbed step results in a large average number of kinks existing along the step (region II, Eqn. 6), then combining Eqns. 5 and 6-region II, we can express the unperturbed step velocity, v_s as:

$$v_s \approx b\left(\frac{2R_{kk}}{R_k}\right)^{1/2} R_k, \quad \text{where} \left(\frac{2R_{kk}}{R_k}\right)^{1/2} = \rho_k \tag{7}$$

In the KD model, a small perturbation in the kink density, $\Delta\rho_k$, leads to a new step velocity, normal to the original step direction, v_s':

$$v_s' = v_s + \Delta\rho_k b R_k \tag{8}$$

In Eqn. 8, we have assumed that the increase in step vicinality, giving rise to a higher density of unidirectional kinks, does not reduce the density of opposing kinks. In a recent step model directed at determining the interpolation function between a straight, close-packed step velocity and a highly vicinal step velocity (Chernov, 1998), a somewhat different function from that of Eqn. 8 was found. From Eqn. 8, the angle θ that the perturbed step forms with the unperturbed direction (see Fig. 8) is defined by:

$$\theta = \tan^{-1}\frac{n_k b}{n_k/\Delta\rho_k} = \tan^{-1}\Delta\rho_k b \tag{9}$$

where n_k is the average number of excess unidirectional kinks present along the step. The KD model can be used to indirectly determine the net kink velocity by combining Eqns. 7–9 above:

$$R_k = v_s'\left(1-\frac{v_s}{v_s'}\right)\cot\theta \tag{10}$$

In contrast, the model by Chernov (1998) leads to the calculation of R_k via Eqn. 11:

$$R_k = v_s'\left(1-\frac{v_s}{v_s'}\right)^{1/2}\cot\theta \tag{11}$$

Equation 10 will always give a value of R_k that is less than that given by Eqn. 11, but for small v_s/v_s', the error is small. This follows from the continuum model treatment of sites parallel to the step edge for Eqn. 10. In arriving at Eqn. 10, it was assumed that

the length, parallel to the step, of a double kink is infinitesimally small. Due to the actual size of atoms and molecules along a step, this assumption is only reasonable for small v_s/v'_s. Equation 11 accounts for this finite size and as a result, the forced kinks on a vicinal step reduce the number of opposing kinks due to the limited density of available sites for kinks to exist. It is clear then that the Chernov (1998) model is more realistic by accounting for the discrete size of the step components. Therefore, we will use Eqn. 11 in the following examination of HAFM results, but Eqn. 10 and the simplified model outlined above provide the necessary visualization of the KD problem.

Once R_k is determined, R_{kk} may be found from Eqn. 6. As an example of the application of this KD model, the terrace labeled "3" in Fig. 6b (90 °C in water) is bounded on the right hand side by a [010] monolayer segment perturbed by a bilayer segment during dissolution in Figs. 6c and 6d. The bilayer step velocity perpendicular to the [010] direction is 0.61 ± 0.06 nm s^{-1} = v_s'. The monolayer step velocity in the same direction is $v_s = 0.41 \pm 0.04$ nm s^{-1}, and the angle $\theta = 7.5 \pm 1.8°$. Using Eqn. 11, the kink velocity is therefore 2.7 ± 0.8 nm s^{-1}. Further, using Eqn. 6-(region II) and $b = 0.888$ nm for barite along [100], the double-kink nucleation rate is $R_{kk} = 0.04 \pm 0.01$ nm^{-1} s^{-1}. Equation 7 then gives a kink density of $\rho_k = 0.17 \pm 0.04$ nm^{-1} or a kink-kink spacing of $\rho_k^{-1} \sim 6 \pm 1$ nm. Although the [010] steps appear straight based on the HAFM images in Fig. 6, the KD model predicts that these steps are rather rough on a scale of 1-10 nm. This roughness scale is at or below the true contact-mode resolution limit of an AFM tip assuming a typical tip radius of 5-10 nm. This example demonstrates the importance of suitable models for step motion due to the lack of direct information provided by AFM images. In contrast, for the [120] monolayer steps, $v'_s = 1.1 \pm 0.1$ nm s^{-1}, $v_s = 0.51 \pm 0.05$ nm s^{-1}, $b = 0.7$ nm and $\theta = 2.1 \pm 1.4°$ where we find the kink-kink spacing to be ~ 30 ± 15 nm at 90 °C. This large spacing implies that the rate of detachment at kink sites, relative to kink nucleation, is much higher on the [120] steps when compared to the [010] steps.

A second application of the KD model is demonstrated from a barite growth example. Figure 9a shows one of several hillocks from Fig. 9b growing at 108 °C. When steps of one growth hillock annihilate with those of the neighboring hillock, an *unbounded* step occurs. Specifically defined for growth conditions, an *unbounded* step is a step that is terminated on one or both ends by internal corners which serve as continuous sites for kink attachment. A *bounded* step is then defined as a step that is terminated at both ends by external corners, as in the steps comprising the upper tiers of the growth hillock in Fig. 9a. The formation of an unbounded step, as illustrated in Fig. 9a, can remove the nucleation barrier to step advance. As a result, the step advances rapidly and at a new angle determined by the density of kinks produced by the step annihilation event. In the KD model, the unbounded step moves at a velocity (normal to the original step direction) that is directly related to the kink velocity. Applying the KD model to measurements of

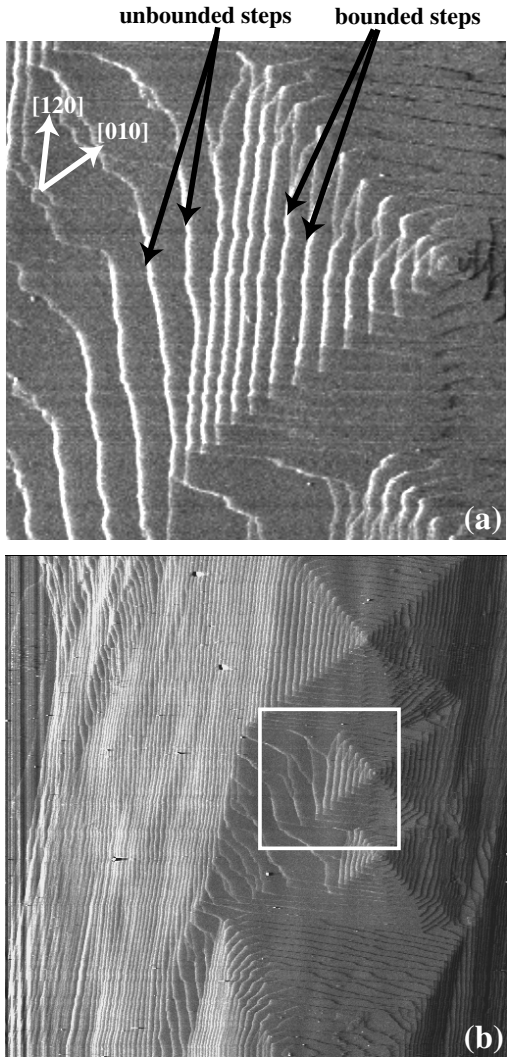


Fig. 9. (a) 5.2 µm x 5.2 µm HAFM image of barite (001) taken at 108 °C with a 20 g/hr flow of supersaturated solution ($\log[(a_{Ba^{2+}} \cdot a_{SO_4^{2-}})/K_{sp}] = 0.155$).

(b) 19 µm x 19 µm HAFM image showing the multiple intersecting growth hillocks in the region surrounding the hillock shown in (a), outlined by the square in (b).

step angles and growth velocities gives $R_k = 4.2 \pm 0.8$ nm s^{-1} and $R_{kk} = 0.10 \pm 0.03$ $nm^{-1}s^{-1}$ by taking $b = 0.7$ nm for the kink depth on the [120] bilayer steps. The kink spacing is then found to be approximately 5 nm on the bounded [120] bilayer steps. As in the dissolution example for the [010] monolayer step, the KD model suggests an atomically rough [120] bilayer step under the above conditions.

AFM observations allow us to better understand kink dynamics along elementary steps on crystal surfaces, and how these dynamics ultimately lead to predictions of kink formation energies and microscopic equilibrium structures. The estimation of rates of kink attachment and/or detachment is useful for evaluating rate laws for elementary reactions at crystal surfaces. For example, kink attachment may be assumed to follow a first-order rate law whereas kink detachment generally follows a zeroth-order rate law:

$$R_k = b(w_+ - w_-) = bw_-\left(\frac{a}{a_{eq}} - 1\right) \qquad (12)$$

In Eqn. 12, R_k is the net kink velocity and is only obtained via models such as the KD model. w_+ and w_- are attachment and detachment frequencies, respectively, a is the experimental activity, and a_{eq} is the equilibrium activity of dissolved growth constituents. To determine w_+ and w_-, it is necessary to obtain data over a range of solute activity or supersaturation. Under local equilibrium conditions, $R_k = 0$, which is impractical to measure with reasonable certainty. However, by determining w_+ and w_- and their temperature dependence, then by applying Eqn. 7 to find the kink density, the kink formation energy, ε, can be determined:

$$\varepsilon = -kT\ln\left(\frac{b\rho_k}{2(a/a_{eq})^{1/2}}\right) \qquad (13)$$

The kinetic barrier to exchange at kink sites as represented by the activation energy for w_+ and w_- when compared to ε, allows us to then discuss the appropriate treatment of step dynamics (e.g., Higgins et al., 2000a) from either a kinetically-determined process, or a process based on equilibrium thermodynamics.

The above examples that we have presented show that it is possible to measure net kink motion within the implicit assumptions of the KD model. The key variable that remains uncontrolled in most dynamic AFM experiments, with few exceptions (e.g., Hong et al., 1997; Coles et al., 1998; Suárez and Compton, 1998), is mass transport near the crystal surface. While very sluggish surface reactions generally are accepted as surface-controlled reactions, there is no easy means of distinguishing between reactions that are slightly too fast to be surface-controlled and reactions that are slow enough to be unaffected by variable or unpredictable fluid flow. We have tested a new hydrodynamic inlet system for the HAFM based on the design of Coles et al. (1997) that allows us to assess the validity of proposed reaction mechanisms obtained by HAFM under known hydrodynamic conditions. A report of our initial results is forthcoming (Higgins et al., submitted).

The above application of a simple approach to determining kink dynamics is an important step toward understanding the *chemical kinetics* of mineral dissolution and growth at the ionic/molecular level. By treating the problem initially through the generic *kink* nomenclature, we may begin to assign relative reactivities to various molecular surface structures. In doing so, we may begin looking toward understanding the reasons for a particular ordering of kink reactivity based on molecular structure, steric effects, nearest neighbor interactions, and edge diffusion. The data presented are truly new data in the sense that they cannot be immediately compared to any existing data. Effective rates of kink motion are only amenable to measurement by high-resolution, in situ observations. Therefore, we must regard these data with objectivity when discussing them in light of the model assumptions that were used to obtain the data. The observations reported here for barite add a new branch of information regarding the kinetics of reactions at this surface in that without the use of elevated temperatures, the molecular kinetics on barite surfaces are far too slow to make AFM measurements under a wide range of solution conditions. In addition to further experiments to test various hypotheses regarding reactivity, this level of detail will require computational tools such as *ab-initio* molecular modeling, molecular dynamics, and Monte Carlo simulations. Computational models may be used to evaluate kink energetics obtained by this experimental approach, such as those results recently reported by Pina et al. (1998).

4. SUMMARY

Both techniques we have presented enable the direct (or, strictly speaking, *more* direct) investigation of interfacial processes and properties that have previously been inferred on the basis of macroscopic stoichiometric equilibrium or rate data. These abilities, used in conjunction with stoichiometric and compositional data, can provide key constraints upon a range of possible mechanistic interpretations and models. Further, these techniques provide data that can be more easily and directly related to macroscopic rates on the one hand, and to molecular-modeling calculations on the other. For example, it is increasingly pos-

sible to use computational approaches to inquire about local surface structures and reactivities (e.g., pertaining to kink sites or to the orientation and structure of water molecules near a surface) and then to relate such calculations directly to HAFM or SHG measurements that must be interpreted on the basis of the same structures and reactivities. These, in turn, can provide mechanistic insight for reactions at mineral surfaces. New techniques are thus allowing us to integrate our understanding of rock-water interaction in a wide variety of geochemically relevant settings across molecular-to-macroscopic scales.

Acknowledgments-We thank Roland Hellmann, Andreas Lüttge, Don Baer, and an anonymous reviewer for helpful suggestions for improving the manuscript. We gratefully acknowledge the support of grants from the National Science Foundation, #EAR-9634143 and #EAR-9725993 to CME, #CHE-9708451 to CME and SRH, the DOE Office of Basic Energy Sciences, #KC040302 to KGK, #DE-FG03-96SF14623/A000 to CME, and the German Academic Exchange Service (DAAD) to GJ.

Editorial Handling: R. Hellmann

REFERENCES

Ainsworth C. C., Friedrich D. M., Gassman P. L., Wang Z., and Joly A. G. (1998) Characterization of salicylate-alumina surface complexes by polarized fluorescence spectroscopy. *Geochim. Cosmochim. Acta* **62**, 595-612.

Bargar J. R., Towle S. N., Brown G. E., and Parks G. A. (1997) XAFS and bond-valence determination of the structures and compositions of surface functional groups and Pb(II) and Co(II) sorption products on single-crystal α-Al_2O_3. *J. Colloid Interface Sci.* **185**, 473-492.

Bhattacharyya K., Sitzmann E. V., and Eisenthal K. B. (1987) Study of chemical reactions by surface second harmonic generation: p-nitrophenol at the air-water interface. *J. Chem. Phys.* **87**, 1442-1443.

Bosbach D. (2002) Linking molecular scale barite precipitation mechanisms with macroscopic crystal growth rates (this volume).

Bosbach D., Hall C., and Putnis A. (1998) Mineral precipitation and dissolution in aqueous solution: in-situ microscopic observations on barite (001) with atomic force microscopy. *Chem. Geol.* **151**, 143-160.

Britt D. W. and Hlady V. (1997) In-situ atomic force microscope imaging of calcite etch pit morphology changes in undersaturated and 1-hydroxyethylidene-1,1-diphosphonic acid poisoned solutions. *Langmuir* **13**, 1873-1876.

Buckley A. N. and Woods R. (1994) On the characterization of sulfur species on sulfide mineral surfaces by X-ray photoelectron-spectroscopy and Raman-spectroscopy. *J. Electroanal. Chem.* **370**(1-2), 295-296.

Burton W. K., Cabrera N., and Frank F. C. (1951) The growth of crystals and the equilibrium structure of their surfaces. *Phil. Trans. Roy. Soc. London* **A243**, 299-358.

Butt H.-J., Kappl M., Mueller H., Raiteri R., Meyer W., and Rühe J. (1999) Steric forces measured with the atomic force microscope at various temperatures. *Langmuir* **15**, 2559-2565.

Casey W. H., Phillips B. L., Karlsson M., Nordin S., Nordin J. P., Sullivan D. J., and Neugebauer-Crawford S. (2000) Rates and mechanisms of oxygen exchanges between sites in the $AlO_4Al_{12}(OH)_{24}(H_2O)_{12}^{7+}$ (aq) complex and water: Implications for mineral surface chemistry. *Geochim. Cosmochim. Acta*, **64**, 2951-2964.

Castro A., Bhattacharyya K., and Eisenthal K. B. (1991) Energetics of adsorption of neutral and charged molecules at the air/water interface by second harmonic generation: Hydrophobic and solvation effects. *J. Chem. Phys.* **95**, 1310-1315.

Cheng L., Lyman P. F., Sturchio N. C., and Bedzyk M. J. (1997) X-ray standing wave investigation of the surface structure of selenite anions adsorbed on calcite. *Surf. Sci.* **382**, L690-L695.

Chernov A. A. (1963a) Crystal growth forms and their kinetic stability. *Sov. Phys. Crystallogr.* **8**, 63-67.

Chernov A. A. (1963b) The kinetics of the growth forms of crystals. *Sov. Phys. Crystallogr.* **7**, 728-730.

Chernov A. A. (1998) Step kinetics by one-dimensional "nucleation". *Materials Sci. Forum* **276-277**, 71-78.

Coles B. A., Compton R. G., Booth J., Hong Q., and Sanders G. H. W. (1997) A hydrodynamic AFM flow cell for the quantitative measurement of interfacial kinetics. *J. Chem. Soc., Chem. Commun.*, 619-620.

Coles B. A., Compton R. G., Suárez M., Booth J., Hong Q., and Sanders G. H. W. (1998) A hydrodynamic atomic force microscopy flow cell for the quantitative measurement of interfacial kinetics: The aqueous dissolution of salicylic acid and calcium carbonate. *Langmuir* **14**, 218-225.

Conboy J. C., Daschbach J. L., and Richmond G. L. (1994) Studies of alkane/water interfaces by total internal reflection second harmonic generation. *J. Phys. Chem.* **98**, 9688-9692.

Corn R. M. and Higgins D. A. (1994) Optical second harmonic generation as a probe of surface chemistry. *Chem. Rev.* **94**, 107-125.

Danielwicz-Ferchmin I. and Ferchmin A. R. (1996) Water density in the double layer. *J. Phys. Chem.* **100**, 17281-17286.

Davis J. A. and Kent D. B. (1990) Surface complexation modeling in aqueous geochemistry. In *Mineral-Water Interface Geochemistry* (eds. M. F. Hochella Jr. and A. F. White). Reviews in Mineralogy vol. 23, Mineralogical Society of America, Washington, D.C. pp. 177-259.

Dove P. M. and Platt F. M. (1996) Compatible real-time rates of mineral dissolution by atomic force microscopy (AFM). *Chem. Geol.* **127**, 331-338.

Du Q., Freysz E., and Shen Y. R. (1994) Vibrational spectra of water molecules at quartz/water interfaces. *Phys. Rev. Lett.* **72**, 238-241.

Eggleston C. M., Hug S., Stumm W., Sulzberger B., and dos Santos Afonso M. (1998) Surface complexation of sulfate by hematite surfaces: FTIR and STM observations. *Geochim. Cosmochim. Acta* **62**, 585-593.

Frank F. C. (1974) Nucleation-controlled growth on a one-dimensional growth of finite length. *J. Cryst. Growth* **22**, 233-236.

Gragson D. E., McCarty B. M., and Richmond G. L. (1997) Ordering of interfacial water molecules at the charged air/water interface observed by vibrational sum frequency generation. *J. Am. Chem. Soc.* **119**, 6144-6152.

Gratz A. J., Hillner P. E., and Hansma P. K. (1993) Step dynamics and spiral growth on calcite. *Geochim. Cosmochim. Acta* **57**, 491-495.

Heinz T. F., Chen C. K., Ricard D., and Shen Y. R. (1982)

Spectroscopy of molecular monolayers by resonant second-harmonic generation. *Phys. Rev. Lett.* **48**, 478-481.

Heinz T. F., Tom H. W. K., and Shen Y. R. (1983) Determination of molecular orientation of monolayer adsorbates by optical second-harmonic generation. *Phys. Rev. A* **28**, 1883-1885.

Higgins D. A., Byerly S. K., Abrams M. B., and Corn R. M. (1991) Second harmonic generation studies of methylene blue orientation at silica surfaces. *J. Phys. Chem.* **95**, 6984-6990.

Higgins D. A., Abrams M. B., Byerly S. B., and Corn R. M. (1992) Resonant second harmonic generation studies of p-nitrophenol adsorption at condensed phase interfaces. *Langmuir* **8**, 1994-2000.

Higgins S. R. and Eggleston C. M. An optical second harmonic generation study of dye molecule sorption at Al_2O_3-water interfaces. *Geochim. Cosmochim. Acta* (submitted).

Higgins S. R., Eggleston C. M., Jordan G., Knauss K. G., and Boro C. O. (1998a) In situ observation of oxide and silicate mineral dissolution by hydrothermal scanning force microscopy: Initial results for hematite and albite. *Mineral. Mag.* **62**, 618-619.

Higgins S. R., Eggleston C. M., Knauss K. G., and Boro C. O. (1998b) A hydrothermal atomic force microscope for imaging in aqueous solution up to 150 °C. *Rev. Sci. Instrum.* **69**, 2994-2998.

Higgins S. R., Jordan G., Eggleston C. M., and Knauss K. G. (1998c) Dissolution kinetics of the barium sulfate (001) surface by hydrothermal atomic force microscopy. *Langmuir* **14**, 4967-4971.

Higgins S. R., Stack A., Eggleston C. M., and Dos Santos Afonso M. (1998d) Proton and ligand adsorption at silica- and alumina-water interfaces studied by optical second harmonic generation (SHG). *Mineral. Mag.* **62**, 616-617.

Higgins S. R., Bosbach D., Eggleston C. M., and Knauss K. G. (2000a) Kink dynamics and step growth on barium sulfate(001): A hydrothermal scanning probe microscopy study. *J. Phys. Chem. B*, **104**, 6978-6982.

Higgins S. R., Boram L., Coles B. A., Compton R. G., Knauss K. G., and Eggleston C. M. Dissolution kinetics, step and surface morphology of magnesite (104) surfaces in acidic aqueous solution at 60 °C by atomic force microscopy under defined hydrodynamic conditions. *J. Phys. Chem. B* (submitted).

Hong Q., Suárez M. F., Coles B. A., and Compton R. G. (1997) Mechanism of solid/liquid interfacial reactions. The maleic acid driven dissolution of calcite: an atomic force microscopy study under defined hydrodynamic conditions. *J. Phys. Chem. B* **101**, 5557-5564.

Hug S. J. and Sulzberger B. (1994) In situ Fourier transform infrared spectroscopic evidence for the formation of several different surface complexes of oxalate on TiO_2 in the aqueous phase. *Langmuir* **10**, 3587-3597.

Jordan G. and Rammensee W. (1998) Dissolution rates of calcite (1014) obtained by scanning force microscopy: Microtopography-based dissolution kinetics on surfaces with anisotropic step velocities. *Geochim. Cosmochim. Acta* **62**, 941-947.

Jordan G., Higgins S. R., Eggleston C. M., Swapp S. M., Janney D. E., and Knauss K. G. (1999) Acidic dissolution of plagioclase. In-situ observations by hydrothermal atomic force microscopy. *Geochim. Cosmochim. Acta* **63**, 3183-3191.

Jordan G., Higgins S. R., Eggleston C. M., Knauss K. G., and Schmahl W. W. Dissolution kinetics of magnesite in acidic aqueous solution. A hydrothermal atomic force microscopy (HAFM) study: Step orientation and kink dynamics. *Geochim. Cosmochim. Acta* (in press).

Kikteva T., Star D., Zhao Z., Baisley T. L., and Leach G. W. (1999) Molecular orientation, aggregation, and order in rhodamine films at the fused silica/air interface. *J. Phys. Chem. B* **103**, 1124-1133.

Laiti E., Persson P., and Öhman L.-O. (1998) Balance between surface complexation and surface phase transformation at the alumina/water interface. *Langmuir* **14**, 825-831.

Lantz J. M., Baba R., and Corn R. M. (1993) Optical second harmonic generation as a probe of electrostatic fields and flatband potential at single-crystal TiO_2 electrodes. *J. Phys. Chem.* **97**, 7392-7395.

Lantz J. M. and Corn R. M. (1994) Electrostatic field measurements and band flattening during electron-transfer processes at single-crystal TiO_2 electrodes by electric field-induced optical second harmonic generation. *J. Phys. Chem.* **98**, 4899-4905.

Lauritzen J. I. (1973) Effect of a finite substrate length upon polymer crystal lamellar growth rate. *J. Appl. Phys.* **44**, 4353-4359.

Liang Y., Baer D. R., McCoy J. M., and LaFemina J. P. (1996) Interplay between step velocity and morphology during the dissolution of $CaCO_3$ surface. *J. Vac. Sci. Tech. A* **14**, 1368-1375.

Lüttge A., Bolton E. W., and Lasaga A. C. (1999) An interferometric study of the dissolution kinetics of anorthite: The role of reactive surface area. *Amer. J. Sci.* **299**, 652-678.

Mizrahi V. and Sipe J. E. (1988) Phenomenological treatment of surface second-harmonic generation. *J. Opt. Soc. Am. B* **5**, 660-667.

Ong S., Zhao X., and Eisenthal K. B. (1992) Polarization of water molecules at a charged interface: second harmonic studies of the silica/water interface. *Chem. Phys. Lett.* **191**, 327-335.

Park N.-S., Kim M.-W., Langford S. C., and Dickinson J. T. (1996) Atomic layer wear of single-crystal calcite in aqueous solution using scanning force microscopy. *J. Appl. Phys.* **80**, 2680-2686.

Parks G. A. (1965) The isoelectric points of solids oxides, solid hydroxides, and aqueous hydroxo complex systems. *Chem. Rev.* **65**, 177-198.

Parks G. A. (1990) Surface energy and adsorption at mineral/water interfaces: An introduction. In *Mineral-Water Interface Geochemistry* (eds. M. F. Hochella Jr. and A. F. White). Reviews in Mineralogy vol. 23, Mineralogical Society of America, Washington, D.C. pp. 133-175.

Pina C. M., Becker U., Risthaus P., Bosbach D., and Putnis A. (1998) Molecular-scale mechanisms of crystal growth in barite. *Nature* **395**, 483-486.

Russell A. E., Lin A. S., and O'Grady W. E. (1993a) In situ far-infrared evidence for a potential dependence of silver-water interactions. *J. Chem. Soc. Faraday Trans.* **89**, 195-198.

Russell A. E., Williams G. P., Lin A. S., and O'Grady W. E. (1993b) Far-infrared synchrotron radiation for in situ studies of the electrochemical interface. *J. Electroanal. Chem.* **356**, 309-315.

Sahai N. and Sverjensky D. A. (1997) Evaluation of internally consistent parameters for the triple-layer model by the systematic analysis of oxide surface titration data. *Geochim. Cosmochim. Acta* **61**, 2801-2826.

Shiraki R., Rock P. A., and Casey W. H. (2000) Dissolution kinetics of calcite in 0.1 M NaCl solution at room temperature: An atomic force microscopic (AFM) study. *Aquatic*

Geochem. **6**, 87-108.
Simpson G. J. and Rowlen K. L. (1999) An SHG magic angle: Dependence of second harmonic generation orientation measurements on the width of the orientation distribution. *J. Am. Chem. Soc.* **121**, 2635-2636.
Stack A. G., Higgins S. R., and Eggleston C. M. (2001) Point of zero charge of a corundum-water interface probed with optical second harmonic generation (SHG) and atomic force microscopy (AFM): Non-stoichiometric approaches to oxide surface charge. *Geochim. Cosmochim. Acta* **65**, 3055-3063.
Suárez M. F. and Compton R. G. (1998) Dissolution of magnesium oxide in aqueous acid: An atomic force microscopy study. *J. Phys. Chem. B* **102**, 7156-7162.
Sverjensky D. A. (1994) Zero-point-of-charge prediction from crystal-chemistry and solvation theory. *Geochim. Cosmochim. Acta* **58**, 3123-3129.
Sverjensky D. A. and Sahai N. (1996) Theoretical prediction of single-site surface-protonation equilibrium constants for oxides and silicates in water. *Geochim. Cosmochim. Acta* **60**, 3773-3798.
Teng H. H., Dove P. M., and DeYoreo J. J. (1999) Reversed calcite morphologies induced by microscopic growth kinetics: Insight into biomineralization. *Geochim. Cosmochim. Acta* **63**, 2507-2512.
Teng H. H., Dove P. M., Orme C. A., and DeYoreo J. J. (1998) Thermodynamics of calcite growth: Baseline for understanding biomineral formation. *Science* **282**, 724-727.
Toney M. F., Howard J. N., Richer J., Borges G. L., Gordon J. G., Melroy O. R., Wiesler D. G., Yee D., and Sorenson L. B. (1994) Voltage-dependent ordering of water molecules at an electrode-electrolyte interface. *Nature* **368**, 444-446.
Wang H., Yan E. C. Y., Borguet E., and Eisenthal K. B. (1996) Second harmonic generation from the surface of centrosymmetric particles in bulk solution. *Chem. Phys. Lett.* **259**, 15-20.
Wang K.-S., Resch R., Dunn K., Shuler P., Tang Y., Koel B. E., and Yen T. F. (2000) Scanning force microscopy study of etch pits formed during dissolution of a barite (001) surface in CDTA and EDTA solutions. *Langmuir* **16**, 649-655.
Westall J. and Hohl H. (1980) A comparison of electrostatic models for the oxide/solution interface. *Adv. Coll. Interface Sci.* **12**, 265-294.
Workman R. K. and Manne S. (2000) Variable temperature fluid stage for atomic force microscopy. *Rev. Sci. Instrum.* **71**, 431-436.
Yan E. C. Y. and Eisenthal K. B. (2000) Rotational dynamics of anisotropic microscopic particles studied by second harmonic generation. *J. Phys. Chem. B* **104**, 6686-6689.
Zangwill A. (1988) *Physics at Surfaces*. Cambridge University Press, Cambridge.
Zhao X., Ong S., and Eisenthal K. B. (1993a) Polarization of water molecules at a charged interface. Second harmonic studies of charged monolayers at the air/water interface. *Chem. Phys. Lett.* **202**, 513-520.
Zhao X., Ong S., Wang H., and Eisenthal K. B. (1993b) New method for determination of surface pKa using second harmonic generation. *Chem. Phys. Lett.* **214**, 203-207.